



Synthesis of Pt-based hollow nanoparticles using carbon-supported Co@Pt and Ni@Pt core–shell structures as templates: Electrocatalytic activity for the oxygen reduction reaction

D.A. Cantane^a, F.E.R. Oliveira^a, S.F. Santos^b, F.H.B. Lima^{a,*}

^a Instituto de Química de São Carlos, Universidade de São Paulo – USP, CP 780, 13560-970 São Carlos – SP, Brazil

^b Centro de Engenharia, Modelagem e Ciências Sociais Aplicadas – UFABC, Rua Santa, Adélia 166, Santo André – SP 09210-170, Brazil



ARTICLE INFO

Article history:

Received 30 October 2012

Received in revised form 24 January 2013

Accepted 25 January 2013

Available online 14 February 2013

Keywords:

Pt hollow electrocatalysts

Core–shell nanoparticles

Oxygen reduction reaction

ABSTRACT

Pt-based hollow nanoparticles were investigated as electrocatalysts for the oxygen reduction reaction (ORR) in acid electrolyte. The electrocatalysts were synthesized via Ni or Co diffusion/dissolution, induced by the vacancy-mediated Kirkendall effect, during electrochemical potential cycling of Ni@Pt and Co@Pt core–shell nanoparticles in acid media. The nanoparticles were characterized by high resolution transmission electron microscopy, *in situ* X-ray absorption spectroscopy and X-ray diffraction measurements. The results show substantial differences in nanoparticle structure/composition and in the activity for the ORR, depending on the nature of the non-noble metal in the nanoparticle core. The Pt hollow nanostructures showed higher specific catalytic activity than that of the state-of-the-art Pt/C electrocatalyst. This was attributed to three main effects: (i) hollow-induced lattice contraction in the multilayer Pt shells, (ii) mismatch-induced lattice contraction of the thick Pt shell by the remaining Ni or Co atoms and (iii) a ligand effect, due to the electronic interaction of Pt with the remaining Ni or Co atoms in the Pt multilayers of the hollow structure. These three effects caused a Pt *d*-band center down-shift, which decreased the adsorption strength of oxygenated reaction intermediates and spectators, thus increasing the ORR rate.

© 2013 Elsevier B.V. All rights reserved.

1. Introduction

Platinum is the best single metal catalyst for the oxygen reduction reaction (ORR) for low temperature polymer electrolyte membrane fuel cells (PEM), in both acid and alkaline electrolytes [1–5]. Aiming at increasing the reaction rate, several bimetallic electrocatalysts composed of Pt and 3d-transition metals (Co, Ni, Fe) have been investigated [6–9]. These electrocatalysts exhibit improved catalytic performance for the ORR when compared to Pt alone, both in terms of mass activity (per g of Pt) or specific activity (per real cm² of Pt) [10–12]. Previous works have shown that the ORR activity of these bimetallic electrocatalysts can be further improved by enriching the surface of the catalyst with Pt (surface segregation), induced by annealing a Pt₃M surface at elevated temperatures [13–15] and/or induced by dissolution of the 3d-transition metal in an acidic environment [16,7]. The enhancement in ORR specific activity was achieved by using the mismatch-induced lattice contraction and/or the ligand effect [17–21]. In this type of electrocatalyst, Pt atoms suffer a significant *d*-band center

down-shift and, therefore, chemisorb oxygenated and spectator species more weakly than pure Pt.

Another strategy to enhance the Pt electrocatalytic activity that has been explored is the so-called de-alloying method [22]. In this procedure, the formation of a Pt “skeleton” surface in a bimetallic particle is achieved via dissolution of the alloying elements, such as Cu, Ni and Co in an acid electrolyte. The increased activity for the ORR has been ascribed to variations in the number and kind of neighbors surrounding the Pt atoms, as well compression or expansion in the Pt–Pt bond distance, which induces a structural change that directly affects the Pt electronic density of occupied states in the Pt 5*d*-band, weakening the adsorption strength of reaction intermediates and spectators.

Furthermore, in order to enhance the Pt catalytic activity and dramatically decrease the total mass of Pt in the electrocatalyst, some works have focused on the study of core–shell nanostructures, in which an ultra-thin platinum shell is either deposited on a noble [23–25] or non-noble/noble metal nanoparticle core [19,26,27]. Therefore, the total mass of Pt is reduced, while the metal core plays an important role in modifying the Pt electronic structure, decreasing the Pt *d*-band center.

The use of core–shell and bi-metallic alloys with non-noble metal in their composition or in their cores (such as Co, Fe, Ni or Cu atoms) as electrocatalysts would be an important way for

* Corresponding author at: Av. Trabalhador Saocarlense, 400, CP 780, CEP 13560-960, São Carlos, SP, Brazil. Tel.: +55 16 3373 8681; fax: +55 16 3373 9952.

E-mail addresses: fabiohbl@iqsc.usp.br, fabiohbl@gmail.com (F.H.B. Lima).

enhancing both the Pt specific catalytic activity and the Pt mass activity for oxygen reduction in fuel cells operating with acid electrolytes [13,28]. However, these materials show a loss of the non-noble metal due to dissolution in acidic media, which would decrease the ligand effect (electronic interaction between Pt and the non-noble metal) and, consequently, the electrocatalytic performance of the electrocatalyst. However, other nanoparticle compositions can be stable upon potential cycling, as in the case of IrNi [29] and AuNi_{0.5}Fe [30] core–shell structures, with Pt deposited in the outermost layer.

In the case of core–shell or bi-metallic structures with unstoppable non-noble metal dissolution, these materials can be used as precursors for the synthesis of noble metal hollow nanoparticles. Recently, Wang et al. [31] and Dubau et al. [32] studied the ORR catalyzed by Ni@Pt/C core–shell nanostructures and Pt₃Co/C alloys, respectively. They revealed the formation of Pt hollow nanoparticles after electrochemical potential cycling in acid media. The authors ascribed the cause of Pt hollow formation to the diffusion of the non-noble metal atoms from the bulk to the surface of the material, induced by the Kirkendall effect on the nanoscale.

The Kirkendall effect is a diffusion mechanism in which there is net mass flow of a faster diffusing species balanced by the opposing flow of vacancies that condense into voids in solids and, therefore, it is responsible for solid-to-hollow conversions [33–36]. The phenomena of solid state diffusion are more frequently described by using a unique diffusion coefficient which describes the migration of one component through the structure of another (which composes the matrix). This is a typical approach to describe the diffusion of a low content solute. When the amount of both components is considerably high, solid state diffusion is usually described using the diffusion coefficients of one species into the other (*i.e.*, diffusivity of component A into component B, D_{AB}, and diffusivity of component B into component A, D_{BA}). These diffusion coefficients are called “intrinsic diffusion coefficients”. In these metallic systems, diffusion might be described through a combination of both intrinsic diffusion coefficients, describing the so-called interdiffusion. In the 1940s, Kirkendall studied interdiffusion using copper–brass diffusion couples and observed that these intrinsic diffusion coefficients usually have different values. Thus, in order to obey the laws of continuity, vacancies are created and migrate in the opposite direction to the net atomic flux caused by the asymmetry of the intrinsic diffusion coefficients during interdiffusion. These vacancies might condense into the solid, creating voids [33,37].

In nanoparticles, if the core species (a non-noble metal) has the faster intrinsic diffusion coefficient, an outward atomic flux is created in response to a reactive environment to which the material is exposed, and this is balanced by an inward flux of vacancies. This effect is also responsible for the dissolution of the non-noble metal in nanoparticles in acid media (or oxide formation on the material surface in the case of alkaline media). As a result, the formation of a Pt structure with a void in the center occurs, forming the so-called hollow nanoparticle. Some amount of the non-noble metal may remain in the hollow wall layers due to the formation of solid solution, in which diffusion, followed by dissolution, is kinetically very low. This would decrease the rate of non-noble metal diffusion/dissolution on the particle surface.

Among the numerous investigations concerning the synthesis of new electrocatalysts for enhancing both the electrocatalytic activity and durability regarding the ORR in PEM fuel cells, hollow nanostructures have shown novel properties for controlling the electrocatalytic activity [36,46]. However, little is known about how the electrocatalytic activity of these nanoparticles is influenced by varying the size, shape and the remaining activity-enhancing non-noble metal components, which is controlled by the nature of the template through which the hollow structure is produced.

In this work, the synthesis and ORR activity of Pt hollow nanoparticles were studied. The effect of two different non-noble metals as cores (Ni and Co) was investigated on the shape and size of the resulting Pt hollow nanoparticle, in addition to their effect on the electrocatalytic activity for the ORR.

2. Experimental

2.1. Synthesis of carbon-supported Ni@Pt and Co@Pt core–shell and Pt hollow nanoparticles

The investigated materials consisted of carbon-supported Pt hollow nanoparticles, synthesized using Ni@Pt/C and Co@Pt/C core–shell nanostructures as templates. The hollow electrocatalysts are represented by Hollow@NiPt/C and Hollow@CoPt/C, indicating that these two materials were synthesized using Ni or Co as metal cores. Commercial carbon-supported Pt nanoparticles (Pt/C E-TEK) were also used for comparison.

The core–shell nanoparticle templates (Ni or Co core and Pt shell) were synthesized with nominal atomic ratios (Ni:Pt and Co:Pt) of 2:1, adapting a previously published method [39]. For the synthesis, appropriate amounts of Ni(NO₃)₂·2H₂O or Co(NO₃)₂·2H₂O (Sigma-Aldrich) were dissolved in *N,N*-dimethylformamide (DMF, Sigma-Aldrich), followed by the addition of high surface area carbon (Vulcan XC-72, Cabot, 250 m² g⁻¹). The resulting suspension was stirred and sonicated for 10 min in air at room temperature. After this, the solution was stirred and heated at 80 °C until complete evaporation of the solvent in a Petri dish. The samples were cooled in air, and the impregnated powders were submitted to thermal treatment conducted in a tubular oven (MAITEC) under an argon atmosphere at 100 °C, for 1 h, then reduced under an H₂ atmosphere at 450 °C for 3 h. At this stage, the Ni/C and Co/C cores were prepared. After cooling the samples in argon to room temperature, the powders were appropriately transferred to a three-neck flask, under an argon atmosphere, containing an appropriate amount of Pt(acac)₂ (Sigma-Aldrich) dissolved in 200 mL of *N,N*-dimethylmethanamide. Subsequently, the solution was stirred and heated under reflux at 120 °C for 1 h under an H₂ atmosphere. After this, the reflux flask was opened for the complete evaporation of the solvent. The decomposition of Pt(acac)₂ occurs at high temperature (120 °C) and, in the presence of H₂, the Pt atoms directly crystallize on the Ni and Co cores. The carbon-supported M@Pt/C electrocatalysts were then filtered, extensively washed and centrifuged with water and ethanol.

For the synthesis of the Pt hollow nanoparticles, a suspension of the metal/C electrocatalyst was prepared by dispersing the core–shell nanoparticle powder in isopropyl alcohol using an ultrasound bath [40]. An aliquot of 100 μL of the dispersed suspension was pipetted onto the surface of a gold foil and dried under vacuum. After the evaporation of the solvent, 100 μL of a diluted Nafion solution (0.05 wt.%, prepared from a 5 wt.% solution, Aldrich) was pipetted onto the surface of the catalyst in order to attach the catalytic particles to the gold foil electrode. This was used as the working electrode in a three-electrode cell configuration. A reversible hydrogen electrode (RHE) and a ring-shaped gold foil were used as the reference and counter electrodes, respectively. The working electrode was submitted to electrochemical potential cycling in 0.5 mol L⁻¹ H₂SO₄ electrolyte, between 0.05 and 1.1 V vs. RHE, and at 10 mV s⁻¹ (100 cycles). During potential excursions to 1.1 V, the “place exchange” mechanism can occur [41], and this accelerates the Ni or Co diffusion/dissolution processes, in order to obtain the hollow nanostructures. This will be further discussed below. The as-prepared Hollow@NiPt/C and Hollow@CoPt/C nanoparticles were collected from the gold foil by immersing the

foil in isopropyl alcohol in an ultrasound bath followed by drying under vacuum for 2 h.

2.2. Electrocatalyst characterization

The resulting catalyst atomic compositions, before and after potential cycling (*i.e.*, core-shell and hollow nanostructures, respectively), were first estimated by X-ray energy dispersive spectroscopy (X-EDS) analysis, using a Zeiss-Leica/LEO 440 model (LEO, UK) scanning electron microscopy (SEM) with a Link Analytical micro-analyser (Isis System Series 200). Structural features were also determined by X-ray diffraction (XRD) measurements, carried out using a RIGAKU Ultima IV diffractometer with Cu K_{α} radiation ($\lambda = 1.54056 \text{ \AA}$), operating at 40 kV and 40 mA. The measured 2θ range was 20° to 100° (with a scan rate of $0.3^\circ \text{ min}^{-1}$).

The nanostructured electrocatalysts were also investigated using scanning transmission electron microscopy (STEM), using a FEI-TECNAL G²F20 field emission microscope operating at 200 kV. The high angle annular dark field (HAADF) detector and X-EDS measurements were used in order to obtain information on the chemical composition of the nanostructures. The HAADF contrast is related to the atomic number (Z-contrast). STEM – X-EDS line scan measurements were performed on some individual nanoparticles before and after potential cycling, aiming to analyze the chemical composition and distribution of the atomic species across the diameter of the particles. Quantitative analyses were performed on the Pt L and the Ni and Co K lines, using the K factor provided by the TIA software.

Samples for STEM analyses were prepared by dispersing the catalyst powders in isopropyl alcohol and submitting the samples to an ultrasonic bath for 5 min. After this, a drop of the suspension was placed onto a thin carbon film supported by standard TEM copper grids (Electron Microscopy Sciences) and dried under vacuum for 12 h.

The electronic features of the metal electrocatalysts were studied by *in situ* X-ray absorption spectroscopy (XAS) measurements in the X-ray absorption near edge structure (XANES) region at the Pt L₃ absorption edge (11,564 eV), the Ni K absorption edge (8333 eV) and the Co K (7709 eV) absorption edge. The experiments were carried out at the D04-XAFS2 beam line of the Brazilian Synchrotron Light Source Laboratory (LNLS, Brazil) using a home-made spectro-electrochemical cell [42]. The counter electrode was formed from a Pt screen cut in the center to allow the free passage of the X-ray beam. The XAS experiments were performed during chronoamperometric measurements with the electrodes polarized at 0.4 and 0.9 V (vs. RHE) in N₂-saturated HClO₄ 0.1 mol L⁻¹ electrolyte. These two potential were selected in order to obtain the XANES spectrum in a region with the absence (0.4 V) and with the presence of adsorbed oxygenated species (0.9 V) originated from the activation of water molecules [32,41]. The results presented here correspond to the average of at least two independent measurements. The catalyst powder samples were measured in transmission mode using ion chambers filled with 20% argon and 80% N₂. A Si(111) single crystal of third-order was used as the monochromator, and was calibrated using pure Pt, Ni foil and Co foil.

The working electrodes for XAS measurements were composed of the electrocatalysts agglutinated with Nafion® (*ca.* 30 wt.%) and containing $6.0 \text{ mg}_{\text{Pt}} \text{ cm}^{-2}$ or $19.0 \text{ mg} (\text{Ni or Co}) \text{ cm}^{-2}$. The mixture was sonicated for 10 min followed by evaporation in air. The powders were then pressed at 25 °C and 1 bar for 3 min onto a disk-shaped carbon paper (TGP-H-060).

The computer program used for the analysis of the XAS data was the WinXAS package [43]. The data analysis was performed according to the procedures described in more detail in the literature [44]. Briefly, the XANES spectra were first corrected for the background absorption by fitting the pre-edge data (from -60 to -20 eV below

the edge) to a linear formula, followed by extrapolation and subtraction from the data over the energy range of interest. Then, the spectra were calibrated for edge position using the second derivative of the inflection point at the edge jump of the data from the reference channel. Finally, the spectra were normalized, taking as the reference the inflection point of one of the EXAFS (extended X-ray absorption fine structure) oscillations [45].

2.3. Electrochemical experiments—electrocatalytic activity for the ORR

For the ORR measurements, a suspension of 2.0 mg mL^{-1} of the metal/C was prepared, dispersing the catalyst powder in isopropyl alcohol using an ultrasound bath [40]. A $20 \mu\text{L}$ aliquot of the dispersed suspension was pipetted onto the top of a glassy carbon disk of a rotating disk electrode (RDE) (5 mm diameter, 0.196 cm^2) and dried under vacuum. This yielded a Pt load of $8.0 \mu\text{g cm}^{-2}$ (Pt/C, E-TEK), $7.2 \mu\text{g cm}^{-2}$ (Co@Pt/C) and $6.0 \mu\text{g cm}^{-2}$ (Ni@Pt/C). After the evaporation of water, $10 \mu\text{L}$ of a diluted Nafion solution (prepared from a 5% solution, Aldrich) were pipetted onto the surface of the catalyst in order to attach the catalytic particles on the disk electrode substrate [40].

The electrochemical measurements were conducted using an Autolab potentiostat (PGSTAT 30). The electrolyte was 0.1 mol L^{-1} HClO₄ (Sigma-Aldrich) prepared using high purity water (Milli-Q, $18.2 \text{ M}\Omega \text{ cm}$). A conventional electrochemical glass cell with a Luggin capillary was equipped with a water jacket in order to maintain the temperature at 25.0 ± 0.1 °C, utilizing a Cole-Parmer Polystat temperature controller. A ring-shaped platinized-Pt foil (high surface area) and a reversible hydrogen electrode (RHE) were used as the counter and reference electrodes, respectively. The electrolyte was saturated with purified N₂ or O₂ gases, depending on the experiment. Cyclic voltammograms were recorded at 50 mV s^{-1} and steady state polarization curves for the ORR were carried out in several rotations at 5 mV s^{-1} , between 0.05 and 1.1 V that is a range of potentials in which the ORR takes place. The kinetic currents at 0.9 V were calculated using $j_k = j/(1 - j/j_L)$, where j is the measured current value at 0.9 V and j_L is the mass transport limiting current at 0.4 V. The specific activities were calculated by dividing the kinetic currents by the electrochemical active obtained from the hydrogen-desorption region of the cyclic voltammograms, considering 0.21 mC cm^{-2} [40]. The mass activities were calculated by dividing the kinetic currents by the total mass of Pt in the nanoparticles [46].

3. Results and discussion

The effect of the nature of the non-noble metal on the particle distribution on the carbon support, particle size and average atomic composition of the Ni@Pt/C and Co@Pt/C templates were investigated by STEM, X-EDS and XRD. Fig. 1 show the representative dark-field (DF) and bright-field (BF)-STEM images for the as-prepared Ni@Pt/C (a) and Co@Pt/C (b) electrocatalysts, respectively. The images reveal different particles sizes when Ni@Pt and Co@Pt were used as the material templates. The particle size distribution histograms, obtained from the microscopy images, are presented in Fig. 2. For Ni@Pt/C, the histogram shows a region with values between 3 and 5 nm, and larger particles with 10 nm. Additionally, the results evidence the presence of particles or particle agglomeration with sizes between 17 and 20 nm. For Co@Pt/C, the histogram shows a region with values between 5 and 13 nm, and larger particles with sizes between 20 and 25 nm. Also in this case, the results show the presence of particle agglomeration, with sizes between 42 and 54 nm.

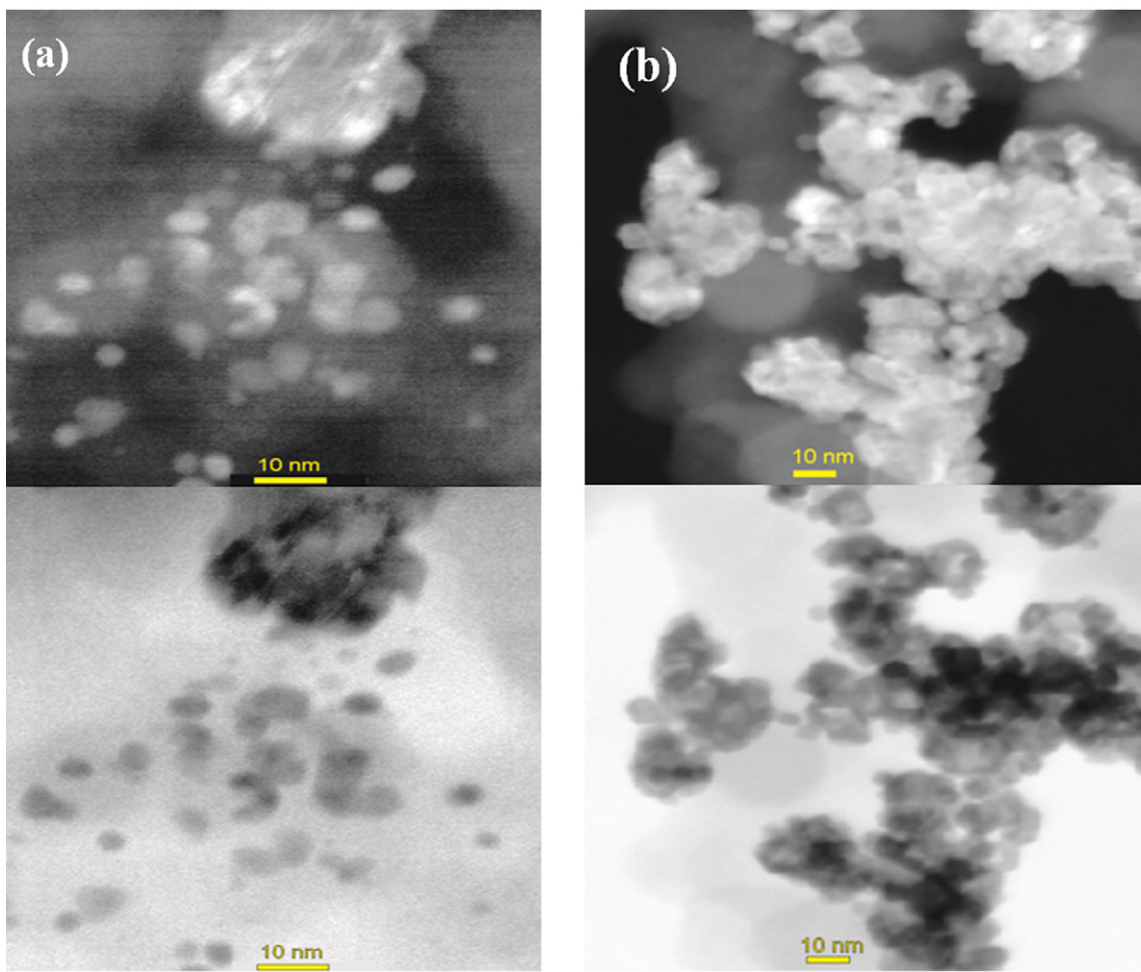


Fig. 1. Annular dark-field (ADF) (top) and bright-field (ABF) (bottom) STEM images for the as-prepared (a) Ni@Pt/C and (b) Co@Pt/C electrocatalysts.

The results of the X-EDS measurements obtained using conventional SEM equipment for the as-prepared and for the cycled nanoparticles are presented in Table 1. As can be noted, the Ni:Pt and Co:Pt atomic ratios in the as-synthesized electrocatalysts were

very close to 1:1 for both materials. The resulting values differed from those of the nominal atomic ratio of 2:1. This can be ascribed to the transmetallation redox phenomenon taking place during the electrocatalyst synthesis. In the step of Ni/C or Co/C immersion into

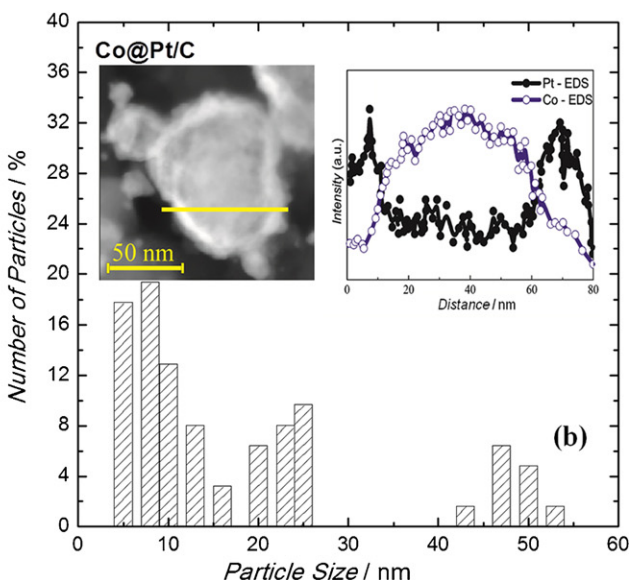
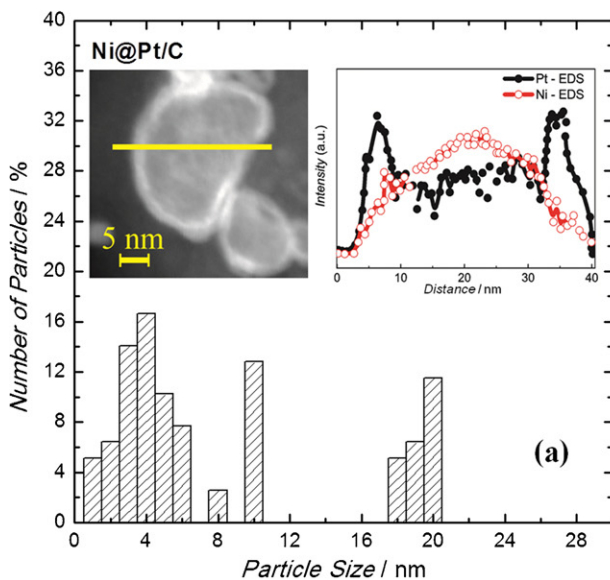


Fig. 2. Particle size distribution histograms for the Ni@Pt/C (a) and Co@Pt/C (b) nanoparticles. Insets: High-angle annular dark field (HAADF) images (left) and their corresponding normalized HAADF intensities of the line-scan X-EDS measurements (right) of selected nanoparticles.

Table 1

Atomic compositions and crystallite sizes obtained by X-ray energy dispersive spectroscopy and X-Ray diffraction experiments.

Samples	EDS (Atomic composition) (Ni:Pt) or (Co:Pt)			XRD (Crystallite size/nm)	
	Nominal composition	Before cycling (as prepared) (core–shell)	After cycling (hollow)	Before cycling (core–shell)	After cycling (hollow)
Ni@Pt/C	2:1	1:1	1:2	3.4	3.6
Co@Pt/C	2:1	1:1	1:9	11.3	11.6

the Pt ion solution, the deposition of Pt^0 can also occur *via* galvanic displacement of metallic Ni or Co atoms from the particle surface, forming Ni^{2+} or Co^{2+} . So, in this case, there is an expected loss of Ni or Co atoms that is comparable to the total amount of Pt atoms deposited *via* galvanic displacement. After producing the Pt hollow nanoparticle *via* electrochemical potential cycling in acidic media, the resulting atomic compositions of the hollow electrocatalysts, also shown in Table 1, were 1:2 (Ni:Pt) and 1:9 (Co:Pt).

As observed in Table 1, the X-EDS measurements revealed that Ni and some amount of Co still remained in the nanoparticle materials even after electrochemical potential cycling. Therefore, in order to determine the location of the Ni, Co and Pt atoms in the as-prepared nanoparticles and in the particles submitted to potential cycling, analyses were conducted using scanning transmission electron microscopy – high-angle annular dark-field (STEM-HAADF) imaging mode. The insets of Fig. 2(a) and (b) shows the HAADF images (left) with their corresponding normalized HAADF intensities of the line-scan X-EDS measurements (right) for selected nanoparticles, for the Ni@Pt/C and Co@Pt/C nanoparticles, respectively. Each measurement (or each curve) of the HAADF intensities was normalized by the largest value obtained, so the maximum intensity value is 1 (this was performed separately for each metal). The HAADF images clearly show a remarkably brighter region in the outer layers and a darker region inside the nanoparticles. This contrast is consistent with an outer shell rich in an element with a higher scattering factor (in our case, Pt) and a core rich in an element with a lower scattering factor (Ni or Co). The normalized HAADF intensity profile for Ni and Co shows that these atoms were homogeneously distributed in the sphere-like core of the nanoparticles. For Pt, the HAADF intensity was high in the particle edge (shell) and decreased in the particle center (core) for both Ni@Pt/C and Co@Pt/C, confirming the formation of core–shell structures for the as-prepared Ni@Pt/C and Co@Pt/C materials. Here, it is important to mention that some line-scan measurements obtained for particle with 5 nm presented similar behavior concerning the atomic composition and distribution. However, the signal to noise ratio was not considerable.

Fig. 3(a) and (b) present the particle size distribution histograms for the materials submitted to the potential cycling (hollow structures). It can be observed that the particle size distributions did not change significantly when compared to those for the as-prepared materials. For Hollow@NiPt/C, the histogram shows a region with values centered at 4 nm nm, and larger particles with 10 nm. Also, the histogram evidences the presence of particles or particle agglomeration with sizes between 18 and 21 nm. For Co@Pt/C, the result shows a region with values between 5 and 13 nm, and larger particles with sizes between 20 and 25 nm. Also in this case, the results show the presence of particle agglomeration, with sizes between 43 and 54 nm. The insets of Fig. 3(a) and (b) present representative HAADF images (left) and the HAADF intensity of the X-EDS line-scan measurements (right) of the Hollow@NiPt/C and Hollow@CoPt/C nanoparticles, respectively. Assessment of the HAADF images reveals a brighter region in the particle shells and a darker region in the nanoparticle cores, confirming the formation of a void region. The HAADF intensities of the line-scan STEM/X-EDS measurements of these particles, presented in Fig. 3 (bottom), indicates a substantial decrease in the Ni and Co content in the

core of the nanoparticles (a contrast similar to the background (carbon)) in Ni@Pt/C and more so in Co@Pt/C nanoparticles, and an enrichment of these metals in the particle shells. On the other hand, the line-scan STEM/X-EDS profile for Pt remained practically unchanged. Although the Ni:Pt and Co:Pt atomic ratios were equal in the as-prepared electrocatalysts, the resulting atomic ratios were considerably different after the potential cycling procedure, *i.e.* 1:2 and 1:9, respectively, as can be observed in Table 1.

The decrease in the amount of Ni and Co atoms in the core of the nanoparticles is associated to their dissolution at the surface, in the acidic electrolyte, followed by their diffusion from the bulk to the nanoparticle surface. This is accelerated by two important events: (i) the increase of the electrode potential or the time given to the oxide film to develop (due to the breaking of the water molecules from the electrolyte) leads to penetration of oxygen into the Pt lattice by interfacial “place exchange” mechanism between Pt atoms and atomic oxygen to form platinum oxide [41]. In this case, the “place exchange” facilitates the corrosion of Ni or Co atoms located in the subsurface region into Ni^{2+} or Co^{2+} ions, which then diffuse into the bulk of the electrolyte [32]; (ii) the dissolution of Co atoms at the surface provides an additional driving force for Ni or Co surface segregation due to the gradient of chemical potential between the bulk and the surface). The differences in the resulting Ni:Pt and Co:Pt atomic ratios, after the 30th cycle, seem to be related with the differences in the Ni and Co chemical reactivity, with Co possessing higher affinity for protons and oxygen (the association with oxygen may occur *via* a place exchange mechanism [41]), producing a faster diffusion/dissolution of Co compared to that of Ni. Here, it is important to mention that, curiously, the resulting atomic ratios changed until the 30th cycle and, after that, they remained constant, even after 100 cycles. The higher stability or the slower dissolution process obtained after the 30th cycle may be associated to a reduced number of lattice vacancies near the particle surface. The inward flux of vacancies to the bulk and the outward flux of Ni or Co from the bulk to the nanoparticle surface may result in a Ni,Pt or Co,Pt solid solution at the hollow shell with a much lower number of lattice vacancies, when compared to that of the as-prepared nanoparticles. Therefore, the diffusion of the Ni or Co has to be performed *via* lattice atomic substitution, in order to reach the surface. This diffusion is kinetically slow and, so, it may account for the stability observed after the 30th potential cycle.

In fact, it was observed that the resulting amount of Ni or Co atoms, after the potential cycling tests, also depends on the homogeneity of the Pt shell covering the non-noble metal cores. It was noted that, for the same amount of Ni or Co atoms, the homogeneity of the Pt shell depends on total amount of Pt ions added during the synthesis. The higher the amount of Pt ions, the higher was the shell thickness and the shell homogeneity. However, as the materials investigated in this work presented a broad size distribution, the obtained shell thicknesses were rather inhomogeneous. Additional X-EDS experiments utilizing Ni@Pt/C particles with inhomogeneous Pt shell thickness surrounding the Ni cores (lower amount of Pt) resulted in Ni:Pt atomic ratio of 1:9, after the potential cycling experiments (same value obtained for the investigated Hollow@CoPt/C material). So, even in the case of using Ni, the synthesis of core–shell nanoparticles presenting a thick and homogeneous Pt shell is essential for a sustained beneficial effect

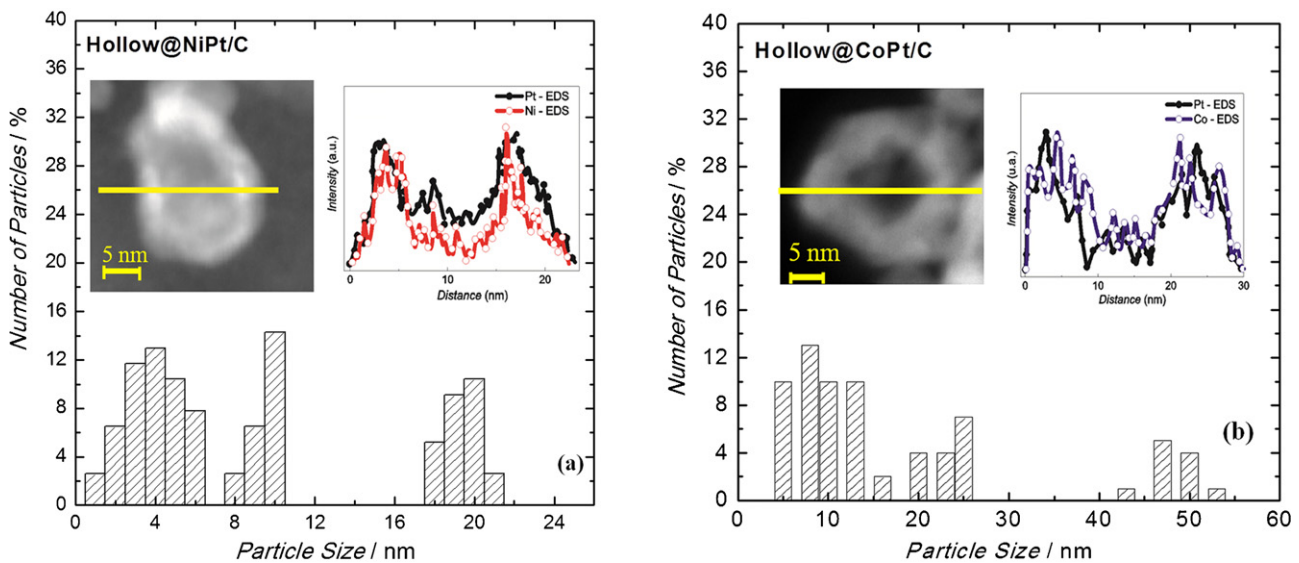


Fig. 3. Particle size distribution histograms for the Hollow@NiPt/C (a) and Hollow@CoPt/C (b) nanoparticles. Insets: High-angle annular dark field (HAADF) images (left) and their corresponding normalized HAADF intensities of the line-scan X-EDS measurements (right) of selected nanoparticles.

induced by the Ni or Co atoms on the electrocatalyst activity for the ORR.

The crystalline structures of the as-prepared (core–shell) and cycled (hollow) electrocatalysts were determined using X-ray diffraction (XRD) measurements, and the results are presented in Figs. 4 and 5. The patterns obtained for Ni/C (before Pt deposition) and for Pt/C were included for comparison. A broad reflection at $2\theta = 25^\circ$, observed in all cases, is due to the carbon support. For both Ni@Pt/C and Co@Pt/C nanoparticles, the five main characteristic peaks of the face-centered cubic (fcc) structure of crystalline Pt can be observed, namely the (1 1 1), (2 0 0), (2 2 0), (3 1 1) and (2 2 2) planes. For the Ni@Pt/C sample, two peaks related to metallic Ni can be observed, but at very low intensities. This may be ascribed to X-ray scattering by the thick Pt layer in the particle shell or due to the formation of a thick layer of Ni–Pt solid solution in the nanoparticle core, as discussed below. For the case of the Co@Pt/C sample, the presence of Co-oxide diffraction peaks can be noted. Additionally, it can be observed that the diffraction peaks for the Co@Pt/C

material are sharper than those for Ni@Pt/C. This feature corroborates with the histograms obtained from the TEM images (Fig. 2(a) and (b)), which show the presence of larger particles for the Co@Pt/C material. Although the presence of small particles for Co@Pt/C is evidenced by the histogram, XRD suffer stronger contribution from the larger ones and, therefore, the resulting diffraction peaks are sharp.

In the as-prepared materials, the Ni and Co atoms may be present mainly in two different locations: (i) to a higher extent in the Ni@Pt/C or Co@Pt/C particle cores or (ii) to a minor extent as segregated nanoparticles. As can be noted in Figs. 4 and 5, after electrochemical potential cycling, the small diffraction peaks related to metallic Ni and those related to Co-oxide completely vanished. This could indicate that the total amount of Ni or Co diminished due to the Kirkendall effect, followed by dissolution, from the core–shell nanoparticles or due to Ni or Co dissolution from segregated phases. Nevertheless, here, it is worth noting that line-scan X-EDS analyses, performed on several different Ni@Pt/C and Co@Pt/C nanoparticles, did not find segregated Ni or Co phases. So, most of the

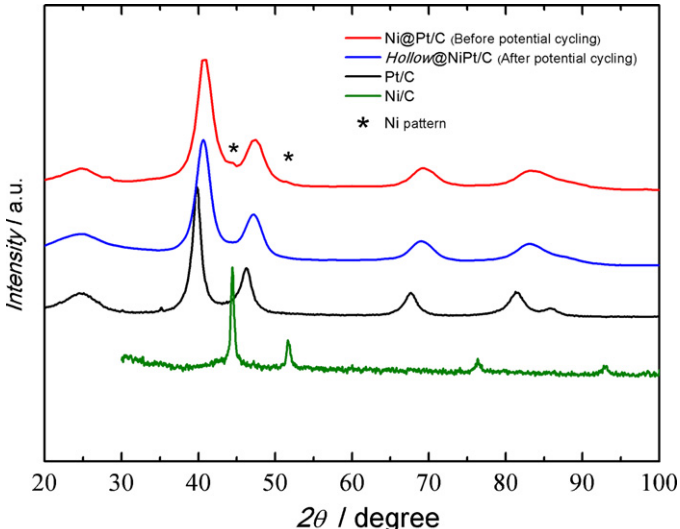


Fig. 4. X-ray powder diffraction intensities for the as-prepared Ni@Pt/C and for the Hollow@NiPt/C nanoparticles. The spectra obtained for Ni/C (before the Pt deposition) and for Pt/C are included for comparison.

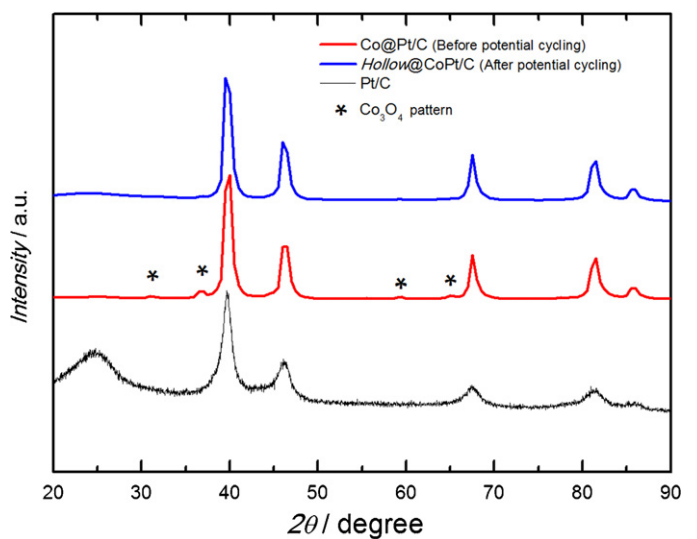


Fig. 5. X-ray powder diffraction intensities for the as-prepared Co@Pt/C and for the Hollow@CoPt/C nanoparticles.

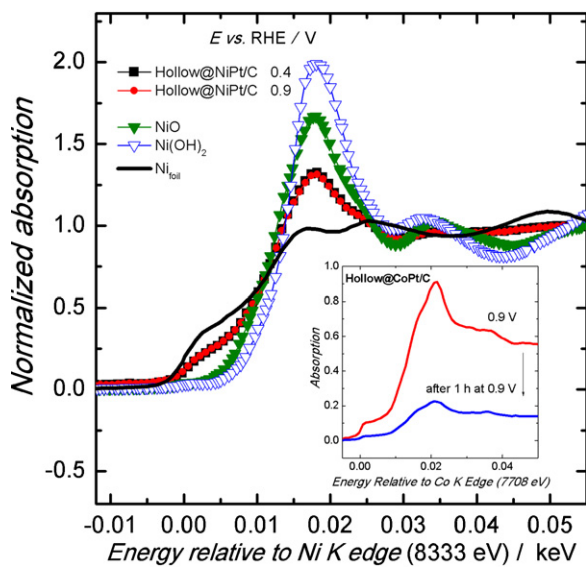


Fig. 6. *In situ* XANES spectra at the Ni K edge for the Hollow@NiPt/C electrocatalysts at 0.4 and 0.9 V in 0.1 mol L^{-1} HClO_4 electrolyte. The *ex situ* spectra obtained for Ni(OH)_2 , NiO and Ni foil reference materials are included for comparison. Inset: *In situ* XANES spectra (non-normalized) at the Co K edge for the Hollow@CoPt/C electrocatalyst obtained just after the polarization at 0.9 V (top), and obtained after 1 h of polarization at 0.9 V in 0.1 mol L^{-1} HClO_4 electrolyte.

metallic Ni and Co atoms are located in the Ni@Pt/C and Co@Pt/C nanoparticle cores. The minor content of Co-oxide may be located on the nanoparticle surface and thus presents higher diffraction peak intensity. Possibly, the Co-oxide phase was formed due to metallic Co oxidation by oxygen in the air on the sites where Pt did not cover the Co atoms.

It can also be noted that the diffraction peaks of the materials were slightly shifted to higher angles relative to those of Pt/C, for both as-prepared (core-shell) and cycled samples (hollow). This indicates Pt lattice contraction due to the presence of Ni or Co atoms in the Pt lattice, forming a solid solution. Probably, this phase is presented as a thick layer, located between the Pt-rich shell and the Ni or Co atoms in the particle core. This would explain why the diffraction peaks from the pure metallic Ni or Co phases were very low or absent. After cycling the core-shell material, in order to produce the Pt hollow nanoparticles, the shift in the diffraction peak angles remained for both cases. This effect may be influenced by two main features. (i) Although there is Ni or Co loss due to dissolution from the particle surface in the acidic electrolyte, the Ni or Co atoms present in the nanoparticle core diffuse to the particle shell *via* the vacancy-mediated Kirkendall effect, and this maintains the altered Pt lattice in relation to that of pure Pt/C. (ii) The Pt lattice parameter is altered from its value as a pure Pt phase due to a significant hollow-induced lattice contraction in the multilayer Pt shells, as also observed in previous works [31,32].

The Pt reactivity in the Hollow@NiPt/C nanoparticles, in the acid electrolyte, as a function of the electrode potential, was investigated *in situ* by the XANES technique. In XANES analysis, the effects of changing the energy of the Pt 5d band and the vacancy are particularly important in electrocatalysis. The formation of vacancies in the metal facilitates the formation of oxygenated species from the activation of water molecules. In the case of the ORR, these species block active sites for the adsorption of oxygen molecules. This will be further discussed below. Fig. 6 shows the *in situ* XANES results obtained at the Ni K edge at $E = 0.4$ and 0.9 V vs. RHE for the Hollow@NiPt/C material. The results obtained for metallic Ni (Ni foil) and for the Ni(OH)_2 and NiO reference oxides are included for comparison. K-edge XANES spectra for 3d transition metals involve

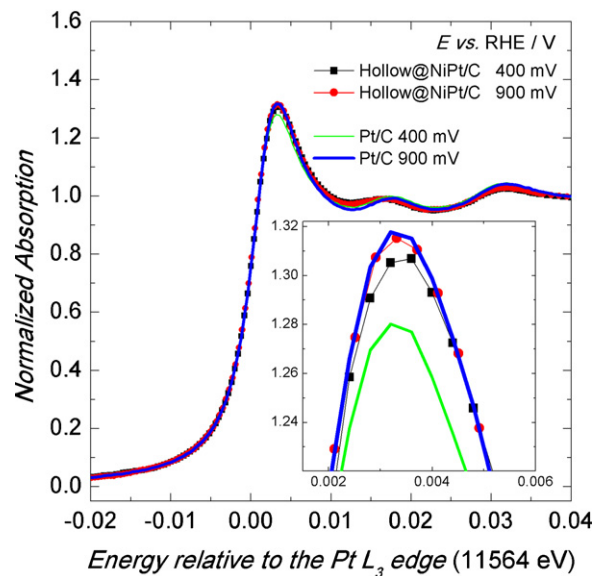


Fig. 7. *In situ* XANES spectra at the Pt L_3 edge for the Hollow@NiPt/C electrocatalysts at 0.4 and 0.9 V in 0.1 mol L^{-1} HClO_4 electrolyte. The *in situ* spectra obtained for Pt/C obtained at the same potentials are included for comparison.

the X-ray induced energy-dependent successive promotion of a 1s electron into valence shells, higher energy bound states and eventually into the continuum. In centrosymmetric bond environments, the lowest energy transitions involving $1s-3d$ excitation is symmetry forbidden and of low intensity (the pre-edge feature at 0.0 eV). On the other hand, for lower symmetries, valence shell d-p mixing allows for enhanced intensity with these transitions and results in the main absorption peak. Observing the XANES spectra for Hollow@NiPt/C, it can be noted that it is situated between the spectra of Ni (metallic) and NiO . The higher absorption intensity of the XANES peak of Ni in the Hollow@NiPt/C material, in relation to that of the Ni foil, may arise from the particle size effect [47] (Ni bulk atoms have a higher coordination number) and from Ni electronic structural modification by the Pt atom, increasing the density of available states (close to the Fermi level) of the Ni atoms, which increases the Ni absorption hump. A similar feature of the Ni XANES spectrum was obtained in a previously published study using a PtNi/C alloy [47]. Another explanation for the higher Ni absorption hump, observed in Fig. 6, could be the formation of NiO at the interface with the Pt shell. This can occur during Ni@Pt/C synthesis, in which NiO is formed in the boundary between the Pt shell and the Ni core, in order to match their lattice parameters, as discussed in the literature [39] ($\text{NiO} = 4.18 \text{ \AA}$, $\text{Ni} = 3.52 \text{ \AA}$ and $\text{Pt} = 3.92 \text{ \AA}$). Another possibility is the formation of NiO through the place-exchange mechanism, which can take place after potential excursions to potentials higher than that of water activation [41].

Here, it is worth mentioning that the magnitude of the Ni XANES main edge, during *in situ* experiments for the Hollow@NiPt/C material conducted at $E = 0.90 \text{ V}$, suffered only a small initial decrease and, after that, did not change over the next 8 h. On the contrary, for the Hollow@CoPt/C material, the XANES magnitude of the Co K edge, with the electrode polarized at 0.9 V , suffered a strong decrease in the initial part of the experiment (1 h), but it remained constant during the next 8 h of polarization at 0.9 V , with very low peak intensity. The non-normalized spectra at the Co K edge for the Co@Pt/C material, obtained at 0.9 V , are presented as an inset of the Fig. 6.

In situ XANES analyses were also carried out at the Pt L_3 edge in order to determine the Pt reactivity or the Pt 5 d-band electronic features in the Hollow@NiPt/C material. Fig. 7 shows the

in situ XANES results for the Hollow@NiPt/C nanoparticle obtained at 0.40 V and 0.9 V vs. RHE. The XANES spectra obtained for Pt/C were included for comparison. The absorption at the Pt L₃ edge (11,564 eV) corresponds to 2p_{3/2-5d} electronic transitions and the magnitude of the absorption hump or white line located at *ca.* 5 eV from the edge is directly related to the Pt 5d electronic occupancy. The higher the hump, the lower the occupancy and *vice versa*. For both Hollow@NiPt/C and Pt/C, it can be seen that the white line magnitude increased with an increase in the electrode potential. This phenomenon is attributed to emptying of the Pt 5d-band, in agreement with the presence of an electron withdrawing effect of the oxygen present in a well-known surface oxide layer formed on the catalyst particle surface above 0.8 V due to water activation [47]. In Fig. 7, it can be seen that, at 0.4 V, the magnitude of the white lines are somewhat higher for the Hollow@NiPt/C material, when compared to those for Pt/C. This provides evidence of the higher density of the available states of the Pt atoms due to Pt electronic structure modification by Ni atoms. On the other hand, an important aspect is that the increase in the magnitude of the white line at 0.9 V, in relation to that at 0.4 V, was higher for Pt/C than that for Hollow@NiPt/C. Thus, the change in the Pt 5 d band, caused by oxide formation on Pt atoms at 0.90 V, is less pronounced for the Pt atoms on the surface of the Ni@Pt/C hollow material, compared to that of Pt/C.

The absorption magnitude of the Pt white line at 0.90 V is also dependent on the relative amount of Pt atoms on the particle surface, with respect to that in the bulk or in the inner layers of the particle (for spherical particles, the lower the particle size, the higher the percentage of atoms on the surface). The higher the amount of Pt atoms on the surface, the higher the number of Pt atoms with adsorbed oxygen species at 0.90 V. So, the smaller enhancement of the Pt 5d white line observed at 0.90 V for the Hollow@NiPt/C nanoparticles, compared to Pt/C, could be a consequence of the larger size of the former catalyst particles (the particle size of the Pt/C E-TEK 20 wt.% is close to 2.5 nm). However, it has to be mentioned that the Hollow@NiPt/C electrocatalyst has a hollow-shaped structure, and this interpretation becomes difficult. Additionally, the smaller white line of Hollow@NiPt/C can be explained based on the electronic interaction between Ni and Pt, which reduces the Pt density of occupied states close to the Fermi level. This electronic modification together with hollow structure leads to a lower Pt d-band center. This reduces the adsorption strength of adsorbates such as OH and/or O from water activation on the Pt surface. [19,47].

3.1. Electrocatalytic activity of the ORR

Fig. 8 shows the cyclic voltammograms (CV) obtained for the Hollow@NiPt/C and Hollow@CoPt/C materials (100th cycle). The CV obtained for Pt/C is included for comparison. The results show the typical behavior regarding the hydrogen and oxide regions for the polycrystalline Pt surface [40,41]. For the investigated hollow catalysts, a lower charge corresponding to the hydrogen under-potential deposition (UPD) region of the CV can be noted in comparison to pure Pt/C. This indicates a reduced Pt surface area or a lower number of electrochemically active Pt atoms on the surface, which is related to the greater particle size, as also shown by the STEM-HAADF images. From the CV curves, Pt surface enrichment with the formation of a Pt thick layer can be also inferred, as no currents associated with non-noble metal oxidation were observed, as pointed out in a previous work [32]. Above 0.75 V, anodic currents were observed for the three different materials; this was ascribed to the breaking of water molecules on the Pt surface, producing Pt-oxide species [41,47]. It is important to mention that the Hollow@NiPt/C and Hollow@CoPt/C CV profiles and their corresponding electrochemical surface areas (ESAs – presented in

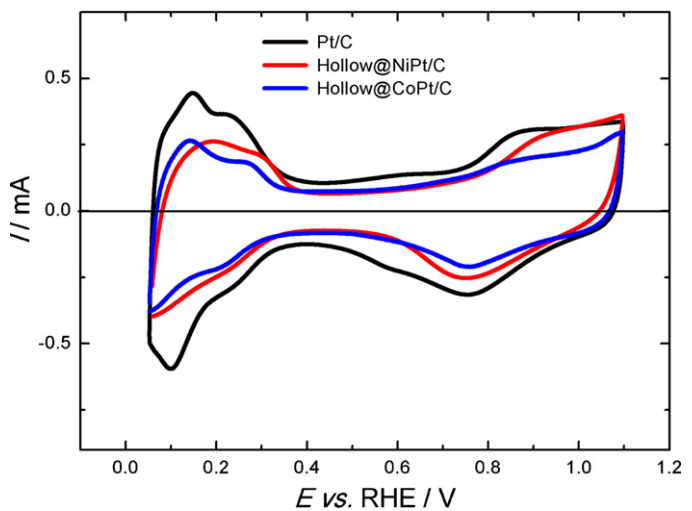


Fig. 8. Cyclic voltammograms obtained for the Hollow@NiPt/C, Hollow@CoPt/C and Pt/C nanoparticles (100th cycle) in N₂-saturated 0.1 mol L⁻¹ HClO₄ electrolyte. Scan rate of 50 mV s⁻¹.

Table 2), calculated using the hydrogen UPD region and considering 210 μC cm⁻², did not change after the 30th cycle, and they remained constant even after 100 potential cycles, from 0.05 to 1.1 V at 0.01 V s⁻¹, for both materials.

The insets of the Fig. 9(a) and (b) show the rotating disk electrode measurements at several rotation speeds for the ORR catalyzed by the Hollow@PtNi/C and Hollow@CoPt/C electrocatalysts, respectively. (The oxygen reduction curves were obtained after 100 voltammetric cycles in another electrochemical cell with 0.1 H₂SO₄ electrolyte in order to produce the hollow structures). The expected increase of the limiting current density in the disk is observed as a function of the rotation speed [48,49]. The disk polarization data at several rotation speeds and electrode potentials were used to construct Koutecky-Levich curves, and the results are also presented in Fig. 9. The evaluation of number of electrons (*n*) involved in the ORR was made taking the Koutecky-Levich plot for the 20 wt.% Pt/C (E-TEK) catalyst in the same conditions as reference, and considering *n* = 4, as observed in previous works [48,49]. The curves at different potentials show a linear dependence at all potentials. The linearity and the parallelism of these plots are usually taken to indicate first order kinetics with respect to molecular oxygen [50]. Additionally, it can be noted that the slopes of the curves for Hollow@NiPt/C and Hollow@CoPt/C are very similar to that for Pt/C, which indicates that the ORR follows, predominantly, the 4-electrons pathway.

The comparison of the steady state polarization curves for the ORR, catalyzed by the Hollow@NiPt/C and Hollow@CoPt/C structures and by Pt/C, obtained at 1600 rpm and 5 mV s⁻¹, is shown in Fig. 10. It can be noted that the ORR limiting current densities assumed close values for these three different nanoparticles, which corroborates with the Koutecky-Levich curves, indicating the predominance of the four-electron pathway in the investigated electrocatalysts [1,2,19]. A higher value of the half-wave potential for Hollow@NiPt/C (*ca.* 0.87 V) can be observed when compared to those values for Hollow@CoPt/C (*ca.* 0.84) and for Pt/C (*ca.* 0.83 V). However, since the total mass of Pt on the electrodes with Hollow@NiPt/C, Hollow@CoPt/C, and Pt/C are different, the specific and mass activities were calculated. The specific activities of these three different electrocatalysts were calculated by dividing the ORR current at 0.90 V by the total active surface area of the electrode, estimated by the charge of the hydrogen UPD region of the CV for each material. The specific activities, presented in Table 2, resulted in values of 0.70, 0.41 and 0.10 mA cm⁻² for Hollow@NiPt/C, Hollow@CoPt/C and Pt/C, respectively, evidencing the superior activity

Table 2

Comparison of the total Pt mass, electrochemical surface areas, half-wave potentials, Pt mass activities, and Pt specific activities for the three different investigated electrocatalysts. The areas were estimated from the hydrogen desorption charges of the CVs, and the Pt specific and mass activities were measured at 0.9 V at 5 mV s^{-1} .

	Pt mass ($\mu\text{g}^{-1} \text{ cm}^2$)	$E_{1/2}$ (V)	ESA ($\text{cm}^{-2} \mu\text{g}^{-1}$)	Pt mass activity ($\text{mA } \mu\text{g}^{-1}$)	Pt specific activity: j_k (0.9 V) (mA cm^{-2})
Hollow@NiPt/C	6.0	0.87	0.61	0.43	0.70
Hollow@CoPt/C	7.2	0.84	0.41	0.17	0.41
Pt/C	9.0	0.83	0.60	0.06	0.10

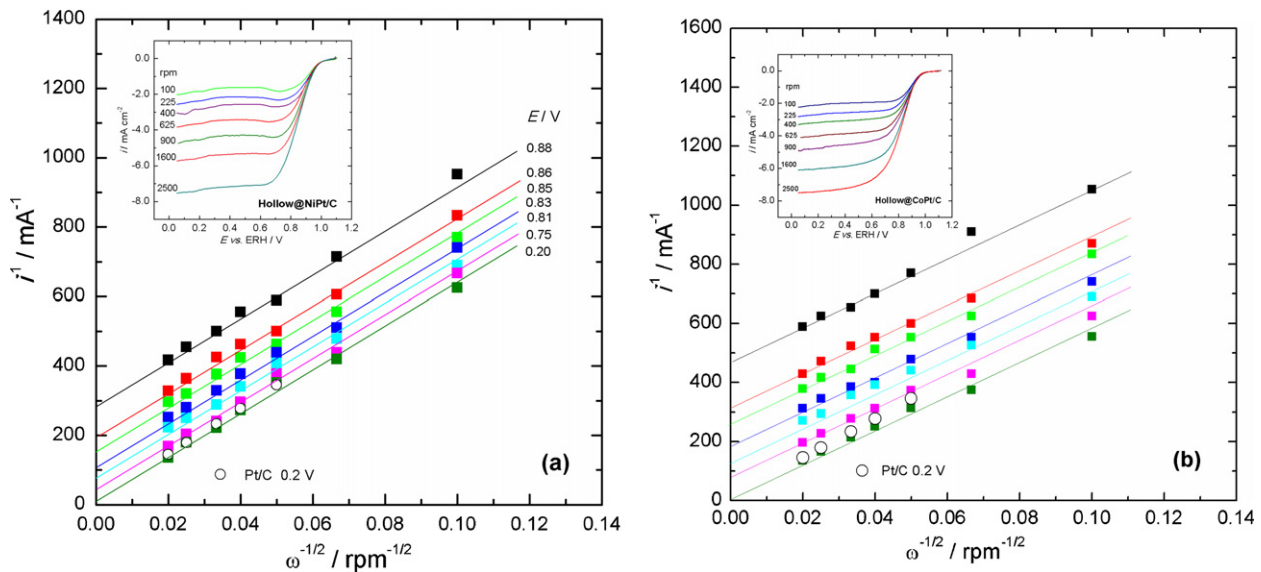


Fig. 9. Koutecky–Levich plots for the ORR catalyzed by the Hollow@NiPt/C (a) and Hollow@CoPt/C (b) at different electrode potentials and rotation rates, in $1.0 \text{ mol L}^{-1} \text{ HClO}_4$ electrolyte. The curve for 20% Pt/C at $E=0.2 \text{ V}$ is included for comparison.

of the hollow materials when compared to that of the state-of-the-art Pt/C electrocatalyst (3 nm). Furthermore, as discussed above, since the different investigated nanoparticles present different values of total mass of Pt in the electrode, the mass activities (current/total mass of Pt) were calculated dividing the ORR current at 0.90 V by the total mass of Pt for each electrode. The values are also presented in Table 2, and were of 0.43, 0.17 and 0.06 $\text{mA } \mu\text{g}_{\text{Pt}}^{-1}$ for Hollow@NiPt/C, Hollow@CoPt/C and Pt/C, respectively.

The oxygen reduction reaction mechanism can be represented as the contribution of two simplified steps: (1) dissociation:

$\text{O}_2 \rightarrow \text{O} + \text{O}$ and (2) hydrogen addition $\text{O} + \text{H} \rightarrow \text{OH}$. Step (1) is favored by strong adsorption, while step (2) is favored by weak adsorption on the catalyst surface. So, a good electrocatalyst for the ORR has to present a balance between these two opposite trends [2,3]. For Pt, previous studies have shown that step (2) is the rate-determining step. So, the Pt d-band center should suffer a down-shift in order to achieve reduced Pt–oxygen adsorption strength. Considering this scenario, the higher specific catalytic activity of the Hollow@NiPt/C and Hollow@CoPt/C electrocatalysts can be attributed to the Pt d-band center down-shift, caused by three main effects: (i) hollow-induced lattice contraction in the multilayer Pt shells, (ii) mismatch-induced lattice contraction of the thick Pt shell by remaining Ni or Co atoms and (iii) a ligand effect, due to the electronic interaction of Pt with the remaining Ni or Co atoms in the Pt multilayers of the hollow structure [17,21,31,32]. These three effects weaken the chemisorption of oxygenated species formed from the reaction intermediates (O or OH) or from spectators (OH from water or anions from the electrolyte), as evidenced by the *in situ* XANES results, which leads to a more facile electro-reduction of the Pt–oxygen species, thereby increasing the ORR rate.

Eventually, even in the case of additional or full dissolution of the non-noble metal (as in the case of the Hollow@CoPt/C, which presented a very low amount of residual Co, and in the case of total dissolution of the non-noble metal, as previously shown [31]) under very long times of operation in a cathode of fuel cells in an acid electrolyte, the enhanced ORR catalytic activity of the Pt hollow nanoparticles is maintained due to the hollow-induced lattice contraction in the multilayer Pt shells, which lowers the Pt d-band center. Therefore, this electrocatalyst structure presents higher specific activity than that of the state-of-the-art Pt/C material, and offers the advantage of higher mass activity, which is favorable for practical applications in fuel cell cathodes.

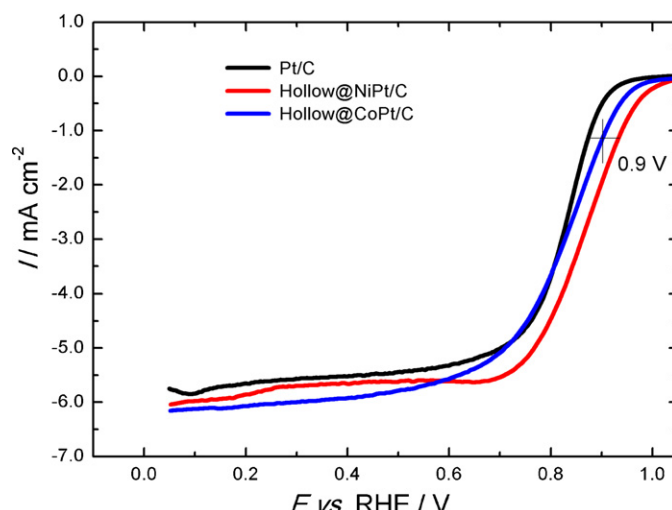


Fig. 10. Steady state polarization curves for the ORR catalyzed by the Hollow@NiPt/C, Hollow@CoPt/C and Pt/C electrocatalysts, obtained at 1600 rpm and 5 mV s^{-1} in O_2 -saturated $0.1 \text{ mol L}^{-1} \text{ HClO}_4$ electrolyte.

4. Conclusions

The results presented in this work show considerable differences in nanoparticle structure/composition and activity for the ORR depending on the nature of the non-noble metal in the nanoparticle core. The Pt hollow nanostructures showed higher specific catalytic activity than that of the state-of-the-art Pt/C electrocatalyst. This was attributed to three main effects: (i) hollow-induced lattice contraction in the multilayer Pt shells, (ii) mismatch-induced lattice contraction of the thick Pt shell by the remaining Ni or Co atoms and (iii) a ligand effect, due to the electronic interaction of Pt with the remaining Ni or Co atoms in the Pt multilayers of the hollow structure. These three effects cause a Pt *d*-band center down-shift, which decreases the adsorption strength of oxygenated reaction intermediates and spectators, thus increasing the ORR rate. The remaining Ni or Co that cause the ligand and lattice contraction effects may be depleted at longer times by Kirkendall effect. Therefore, the total dissolution of Ni or Co will eliminate the ligand effect, but the hollow@Pt/C structure will still present higher activity than that of state-of-the-art Pt/C due to the hollow-induced lattice contraction. As the Ni or Co dissolution during the potential cycling may affect a polymer electrolyte membrane, such as Nafion, the hollow structures should be prepared, by potential cycling, in a separated electrochemical cell (liquid electrolyte) before using the powder electrocatalyst in a real fuel cell. As a final remark, it is worth to mention that this electrocatalyst structure presented higher specific activity than that of the state-of-the-art Pt/C material, and offers the advantage of higher mass activity, which is favorable for practical applications in fuel cell cathodes.

Acknowledgements

The authors thank FAPESP (Fundação de Amparo à Pesquisa do Estado e São Paulo) (Grants: 2009/07629-6, 2011/50727-9 and 2009/11073-3) and CNPq (Conselho Nacional de Desenvolvimento Científico e Tecnológico) for financial support and LNLS (Brazilian Synchrotron Light Laboratory) for assisting with the XAS experiments.

References

- [1] E. Yeager, *Electrochimica Acta* 29 (1984) 1527–1537.
- [2] Zhang F J., M.B. Vukmirovic, Y. Xu, M. Mavrikakis, R.R. Adzic, *Angewandte Chemie International Edition* 44 (2005) 2132–2135.
- [3] F.H.B. Lima, J. Zhang, M.H. Shao, K. Sasaki, M.B. Vukmirovic, E.A. Ticianelli, R.R. Adzic, *Journal of Physical Chemistry C* 111 (2007) 404–410.
- [4] V. Stamenkovic, B.S. Mun, K.J.J. Mayrhofer, P.N. Ross, N.M. Markovic, J. Rossmeisl, J. Greeley, J.K. Nørskov, *Angewandte Chemie* 118 (2006) 2963–2967.
- [5] H.A. Gasteiger, S.S. Kocha, B. Sompalli, F.T. Wagner, *Applied Catalysis B: Environmental* 56 (2005) 9–35.
- [6] C. Wang, N.M. Markovic, V.R. Stamenkovic, *ACS Catalysis* 2 (2012) 891–898.
- [7] P. Mani, R. Srivastava, P. Strasser, *Journal of Power Sources* 196 (2011) 666–673.
- [8] F.H.B. Lima, J.R.C. Salgado, E.R. Gonzalez, E.A. Ticianelli, *Journal of the Electrochemical Society* 154 (2007) 369–375.
- [9] U.A. Paulus, A. Wokaun, G.G. Scherer, T.J. Schmidt, V. Stamenkovic, V. Radmilovic, N.M. Markovic, P.N. Ross, *Journal of Physical Chemistry B* 106 (2002) 4181–4191.
- [10] F. Maillard, M. Martin, F. Gloaguen, J.M. Léger, *Electrochimica Acta* 47 (2002) 3431–3440.
- [11] S. Chen, P.J. Ferreira, W.C. Sheng, N. Yabuuchi, L.F. Allard, Y. Shao-Horn, *Journal of the American Chemical Society* 130 (2008) 13818–13819.
- [12] F.H.B. Lima, J. Zhang, M.H. Shao, K. Sasaki, M.B. Vukmirovic, E.A. Ticianelli, R.R. Adzic, *Journal of Solid State Electrochemistry* 12 (2008) 399–407.
- [13] V.R. Stamenkovic, B.S. Mun, K.J.J. Mayrhofer, P.N. Ross, N.M. Markovic, *Journal of the American Chemical Society* 128 (2006) 8813–8819.
- [14] A. Ruban, H.L. Skriver, J.K. Nørskov, *Surface segregation energies in transition-metal alloys*, *Physical Review B* 59 (24) (1999) 15990–16000.
- [15] U. Bardi, A. Atrei, E. Zanazzi, G. Rovida, P. Ross, *Vacuum* 41 (1990) 437–440.
- [16] M. Oezaslan, P. Strasser, *Journal of Power Sources* 196 (2011) 5240–5249.
- [17] V.R. Stamenkovic, B. Fowler, B.S. Mun, G.F. Wang, P.N. Ross, C.A. Lucas, N.M. Markovic, *Science* 315 (2007) 493–497.
- [18] J. Greeley, I.E.L. Stephens, A.S. Bondarenko, T.P. Johansson, H.A. Hansen, T.F. Jaramillo, J. Rossmeisl, I. Chorkendorff, J.K. Nørskov, *Nature Chemistry* 1 (2009) 552–556.
- [19] F.H.B. Lima, J.F.R. de Castro, L.G.R.A. Santos, E.A. Ticianelli, *Journal of Power Sources* 190 (2009) 293–300.
- [20] J.R. Kitchin, J.K. Nørskov, M.A. Bartea, J.G. Chen, *Physical Review Letters* 91 (2004) 156801-1–156801-4.
- [21] J.R. Kitchin, J.K. Nørskov, M.A. Bartea, J.G. Chen, *Journal of Chemical Physics* 120 (2004) 10240–10246.
- [22] S. Koh, P. Strasser, *Journal of the American Chemical Society* 129 (2007) 12624–12625.
- [23] J. Zhang, Y. Mo, M.B. Vukmirovic, R. Klie, K. Sasaki, R.R. Adzic, *Journal of Physical Chemistry B* 108 (2004) 10955–10964.
- [24] R. Lin, H. Zhang, T. Zhao, C. Caoa, D. Yang, J. Ma, *Electrochimica Acta* 62 (2012) 263–268.
- [25] F.H.B. Lima, E.R. Gonzalez, *Applied Catalysis B: Environmental* 79 (2008) 341–346.
- [26] J. Zhang, F.H.B. Lima, M.H. Shao, K. Sasaki, J.X. Wang, J. Hanson, R.R. Adzic, *Journal of Physical Chemistry B* 109 (2005) 22701–22704.
- [27] K. Hartl, K.J.J. Mayrhofer, M. Lopez, D. Goia, M. Arenz, *Electrochemistry Communications* 12 (2010) 1487–1489.
- [28] F.H.B. Lima, W. Lizcano-Valbuena, E. Teixeira-Neto, E.R. Gonzalez, F.C. Nart, E.A. Ticianelli, *Electrochimica Acta* 52 (2006) 385–393.
- [29] K.A. Kuttiyiel, K. Sasaki, Y.M. Choi, D. Su, P. Liu, R.R. Adzic, *Energy & Environment Science* 5 (2012) 5297–5304.
- [30] K. Gong, D. Su, R.R. Adzic, *Journal of the American Chemical Society* 132 (2010) 14364–14366.
- [31] J.X. Wang, C. Ma, Y.M. Choi, D. Su, Y. Zhu, P. Liu, R. Si, M.B. Vukmirovic, Y. Zhang, R.R. Adzic, *Journal of the American Chemical Society* 133 (2011) 13551–13557.
- [32] L. Dubau, J. Durst, F. Maillard, L. Guétaz, M. Chatenet, J. Andre, E. Rossinot, *Electrochimica Acta* 56 (2011) 10658–10667.
- [33] A.D. Smigelakas, E.O. Kirkendall, *Transactions of AIME* 171 (1947) 130.
- [34] J.G. Railsback, A.C. Johnston-Peck, J. Wang, J.B. Tracy, *ACS Nano* 4 (2010) 1913–1920.
- [35] Y. Yang, L. Liu, F. Guder, A. Berger, R. Scholz, O. Albrecht, M. Zacharias, *Angewandte Chemie International Edition* 50 (2011) 10855–10858.
- [36] Y. Yin, R.M. Rioux, C.K. Erdonmez, S. Hughes, G.A. Somorjai, A.P. Alivisatos, *Science* 304 (2004) 711–714.
- [37] H. Mehrer, *Diffusion in Solids: Fundamentals, Methods, Materials, Diffusion-Controlled Processes*, Springer-Verlag, Berlin, 2007.
- [38] S. Sao-Joa, S. Giorgio, J.M. Penisson, C. Chapon, S. Bourgeois, C. Henry, *Journal of Physical Chemistry B* 109 (2005) 342–347.
- [39] T.J. Schmidt, H.A. Gasteiger, G.D. Stab, P.M. Urban, D.M. Kolb, R.J. Behm, *Journal of the Electrochemical Society* 145 (1998) 2354–2358.
- [40] B.E. Conway, *Progress in Surface Science* 49 (1995) 331–452.
- [41] J.G. McBreen, W.E. O'Grady, K.I. Pandya, R.W. Roffman, D.E. Sayers, *Langumuir* 3 (1987) 428–433.
- [42] T. Ressler, *Journal de Physique IV* 7 (1997), pp. C2-269–C2-270.
- [43] H. Wendt, *Reports on Progress in Physics* 67 (2004) 2105–2181.
- [44] R.Sousa Jr., F. Colmati, E.G. Ciapina, E. Rafael Gonzalez, *Journal of Solid State Electrochemistry* 11 (2007) 1549–1557.
- [45] Y. Zhang, C. Ma, Y. Zhu, R. Si, Y. Cai, J.X. Wang, R.R. Adzic, *Catalysis Today* 202 (2013) 50–54.
- [46] S. Mukerjee, S. Srinivasan, M.P. Soriaga, *Journal of the Electrochemical Society* 142 (1995) 1409–1422.
- [47] J. Perez, E.R. Gonzalez, E.A. Ticianelli, *Electrochimica Acta* 44 (1998) 1329.
- [48] J. Perez, A.A. Tanaka, E.R. Gonzalez, E.A. Ticianelli, *Journal of the Electrochemical Society* 141 (1998) 431.
- [49] N.A. Anastasijevic, V.B. Vesovic, R.R. Adzic, *Journal of Electroanalytical Chemistry* 229 (1987) 305–317.